

Research Paper

Concurrent visual and acoustic tracking of passive and active delivery of nanobubbles to tumors

Carly Pellow^{1,2,3,✉}, Eric C. Abenojar⁴, Agata A. Exner⁴, Gang Zheng^{1,2}, David E. Goertz^{1,3}

1. Department of Medical Biophysics, University of Toronto, Toronto, Ontario, Canada.
2. Princess Margaret Cancer Research Centre, Toronto, Ontario, Canada.
3. Sunnybrook Research Institute, Toronto, Ontario, Canada.
4. Department of Radiology, Case Western Reserve University, Cleveland OH 44106, United States

✉ Corresponding author: Carly Pellow. E-mail: carly.pellow@mail.utoronto.ca

© The author(s). This is an open access article distributed under the terms of the Creative Commons Attribution License (<https://creativecommons.org/licenses/by/4.0/>). See <http://ivyspring.com/terms> for full terms and conditions.

Received: 2020.07.30; Accepted: 2020.09.10; Published: 2020.09.23

Abstract

Background: There has been growing interest in nanobubbles for their potential to extend bubble-mediated ultrasound approaches beyond that of their larger microbubble counterparts. In particular, the smaller scale of nanobubbles may enable them to access the tumor extravascular compartment for imaging and therapy in closer proximity to cancer cells. Compelling preliminary demonstrations of the imaging and therapeutic abilities of nanobubbles have thus emerged, with emphasis on their ability to extravasate. However, studies to date rely on indirect histologic evidence that cannot confirm whether the structures remain intact beyond the vasculature – leaving their extravascular potential largely untapped.

Methods: Nanobubble acoustic scattering was assessed using a recently reported ultra-stable formulation at low concentration (10^6 mL⁻¹) and frequency (1 MHz), over a range of pressures (100-1500 kPa) in a channel phantom. The pressure-dependent response was utilized as a basis for *in vivo* experiments where ultrasound transmitters and receivers were integrated into a window chamber for simultaneous intravital multiphoton microscopy and acoustic monitoring in tumor-affected microcirculation. Microscopy and acoustic data were utilized to assess passive and active delivery of nanobubbles and determine whether they remained intact beyond the vasculature.

Results: Nanobubbles exhibit pressure-dependent nonlinear acoustic scattering. Nanobubbles are also found to have prolonged acoustic vascular pharmacokinetics, and passively extravasate intact into tumors. Ultrasound stimulation of nanobubbles is shown to actively enhance the delivery of both intact nanobubbles and shell material, increasing their spatial bioavailability deeper into the extravascular space. A range of acute vascular effects were also observed.

Conclusion: This study presents the first direct evidence that nanobubbles passively and actively extravasate intact in tumor tissue, and is the first to directly capture acute vascular events from ultrasound-stimulation of nanobubbles. The insights gained here demonstrate an important step towards unlocking the potential of nanobubbles and extending ultrasound-based applications.

Key words: extravasation, intravital imaging, multiphoton microscopy, nanobubble, ultrasound

Introduction

Microbubbles have been in clinical use for decades as biomedical ultrasound contrast agents, with global approval for echocardiography and sanctioning in numerous countries for breast, kidney, liver, spleen, pancreas, gastrointestinal, and urogenital imaging [1, 2]. Current formulations are

comprised primarily of bubbles approximately 1-10 μ m in diameter, with thin compliant shells encapsulating a high molecular weight gas core [3]. Upon systemic injection, microbubbles circulate within the vasculature and oscillate in response to ultrasound resulting in distinct acoustic signatures

which are exploited for imaging contrast [4]. For example, at sufficiently high pressures, the bubbles' volumetric oscillations scatter energy coupled into frequency bands at integer multiples, or harmonics, of the driving frequency. Beyond imaging, sufficiently large oscillations can induce an array of therapeutically relevant biological effects, ranging from transiently increasing microvascular permeability to sustained microvascular damage [5].

Recently, there has been growing interest in submicron ultrasound cavitation agents to extend ultrasound-mediated applications. Submicron agents are of a size that permits higher number densities which can present advantages for high frequency ultrasound imaging, where the focal volume is reduced relative to conventional diagnostic frequencies [6]. Little work has been done from a therapeutic perspective, though initial evidence indicates that submicron formulations can permeabilize the blood-brain-barrier [7, 8] and enhance drug delivery to tumors [9-15]. Importantly, if the agents are sufficiently small they can further gain access to the extravascular compartment of tumors [16], which is accompanied by a host of advantages. From an imaging perspective, extravasated nanobubbles (NBs) can potentially enable detection of leakage associated with disease processes as well as facilitate detection of cell-surface markers in tissue. From a therapeutic standpoint, extravascular NBs can be stimulated by ultrasound for cavitation-based therapy in closer proximity to target cells and presents an opportunity for sonodynamic therapy. Further, nanoparticles exhibit structural versatility, improved pharmacokinetics, and multifunctionality. Shrinking conventional ultrasound contrast agents to the nanoscale consolidates with them the abilities of traditional nanoparticles, bringing new possibilities [16]. Broadly, this class of submicron ultrasound agents [16] includes echogenic liposomes [17-19], polymersomes [20], gas vesicles [21-23], cavitation seeds [14, 24], nanodroplets [15, 25, 26], and nanobubbles [27-29].

Here we focus on NBs, consisting of encapsulated bubbles on the order of hundreds of nanometers. NBs have been shown to be present in large quantities in clinical microbubble formulations [30], though their potential has been largely untapped. Numerous reports have begun to emerge for the formulation of stable NBs [31-35] with applications of conventional ultrasound contrast imaging [34-41], targeted imaging [42-44], and as predictive markers [40, 45]. Several reports have further demonstrated compelling therapeutic evidence of targeted [9-11, 46-48] and loaded [8-13,

46-49] NBs with both passive and active (ultrasound-triggered) approaches.

Despite this growing body of research, works employ ultrasound parameters with little or no basis on NB acoustic scattering, and – though intact extravasation is crucial to many future applications – rely on indirect histologic or macro-scale ultrasound imaging evidence. In this work we employ a fluorescently tagged version of a recently reported ultra-stable NB formulation [34]. We first investigate the scattering response of NBs in a vessel phantom and demonstrate their ability to exhibit distinct nonlinear activity that persists. We then employ a custom dorsal window chamber apparatus to achieve simultaneous intravital multiphoton microscopy optical and acoustic monitoring [50] of NBs in tumor-affected vasculature. Using phantom scattering insights as a rational basis for parameter selection, visual observations are complemented by acoustic pharmacokinetic analysis to demonstrate that these NBs display prolonged stability, circulating in the vasculature for 20 minutes prior to dissolution. We then provide direct confirmation of shell material and intact NBs in the extravascular space after passive intravenous injection. To assess the ability of NBs to actively enhance microvascular permeability, ultrasound is then applied during NB injection and the resultant spatiotemporal extravasation profile and acute vascular effects are assessed. It is demonstrated that ultrasound-stimulated NBs extravasate intact with greater spatial bioavailability for extended imaging and therapeutic applications beyond the vasculature.

Materials and Methods

Agent preparation

Texas Red-labeled NBs were formulated using a modified version of a previously reported technique (developed and characterized *in vitro* and *in vivo* with a clinical scanner in [34]). To prepare the base lipid solution, 144 μL of N-(Texas Red sulfonyl)-1,2-dihexadecanoyl-*sn*-glycero-3-phosphoethanolamine, triethylammonium salt (dissolved in chloroform to a concentration of 1 mg/mL; Texas Red® DHPE; Biotium, Inc.) was first added to a glass vial. The chloroform was then evaporated off in a hot water bath. Next, 6.1 mg of 1,2-dibehenoyl-*sn*-glycero-3-phosphocholine (DBPC C22; Avanti Polar Lipids Inc.), 2 mg of 1,2-dipalmitoyl-*sn*-glycero-3-phosphoethanolamine (DPPE, Corden Pharma), 1 mg of 1,2-dipalmitoyl-*sn*-glycero-3-phosphate (DPPA; Corden Pharma), and 1 mg of 1,2-distearoyl-*sn*-glycero-3-phosphoethanolamine-*N*-[

methoxy(polyethylene glycol)-2000] (DSPE-mPEG2k; Laysan Lipids) were added to the glass vial and dissolved into 0.1 mL of propylene glycol by heating at 80 °C and sonicating. A mixture of 0.1 mL glycerol and 0.8 mL phosphate buffer solution heated to 80 °C was then added, and the resulting lipid solution was sonicated for 10 min at room temperature. The solution was then transferred to a 3 mL glass vial, capped with a rubber septum and aluminum seal, and sealed with a vial crimper. Air was removed from each vial with a 30 mL syringe, and replaced with octafluoropropane gas (C₃F₈, Electronic Fluorocarbons). Samples were activated by high shear gas dispersion in a VialMix (Bristol-Myers Squibb Medical Imaging Inc.) for 45 s. NBs were then isolated by differential centrifugation at 50 g for 5 min with the vial inverted, and 500 µL of NB solution was withdrawn at 5 mm from the bottom with a 21 G needle. Excess Texas Red® DHPE dye was removed by passing the isolated NB solution through a Sephadex PD-10 column (Cytiva). NBs were then transferred to new vials filled with octafluoropropane gas, capped, and sealed. As in a previously explored storage technique, sample vials were frozen and stored at -80 °C until use [51].

Prior to experiments, sample vials were thawed at room temperature. Agent was gently mixed, inverted, and 0.3 mL was extracted with a blunt 18 G needle into 0.7 mL saline. The diluted sample was passed gently through a 0.8 µm pore size syringe filter (Millipore Millex-GV) to isolate the NB population for use within 30 min after thawing. The agent size distribution was measured with a 10 µm aperture Multisizer 4e (Beckman Coulter Inc.) after thawing, filtration and dilution (Figure 1) to have a concentration of 8×10^8 mL⁻¹ and number and volume distribution modes of 0.303 and 0.392 µm, respectively (n = 3 vials).

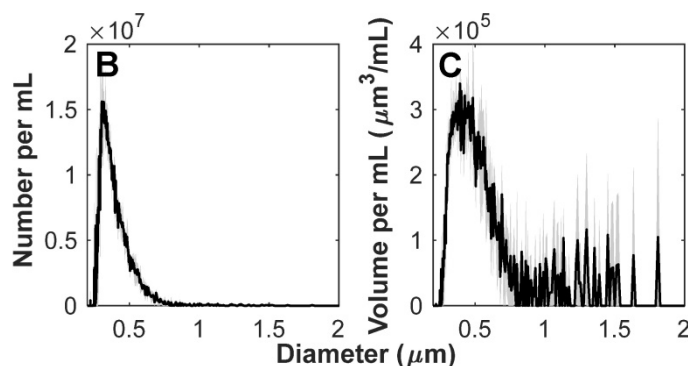
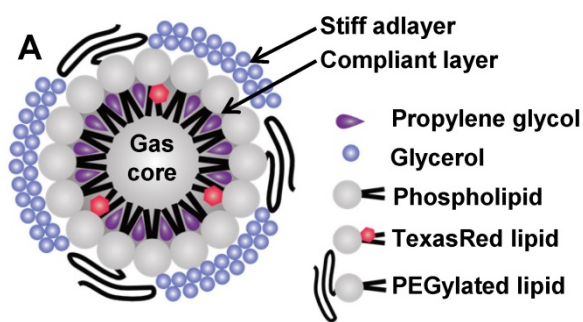


Figure 1. Characterization of nanobubbles. (A) Concept sketch of nanobubbles stabilized by a stiff adlayer of glycerol and compliant layer of propylene glycol. The agent was characterized with a Multisizer 4e (10 µm aperture) to have (B) number and (C) volume distribution modes of 0.303 and 0.392 µm, with a concentration of 8×10^8 mL⁻¹. Mean values (n = 3) are displayed with standard deviations in gray shading.

Benchtop acoustic scattering studies

NB acoustic scattering was assessed at a low concentration of 10^6 mL⁻¹ in a vessel phantom. The phantom consisted of a 0.5 mm diameter channel cast with a needle in an acrylic chamber (3 cm x 3 cm circular cross-section; 1 cm length; 5 mm from the front face) filled with 2 % agar gel, held by mylar sheets (Figure 2A). Upon gelation, the needle was removed to create a channel, and the mylar was removed from the front face to minimize reflections. The phantom was placed in a degassed water bath such that each transducer (two were utilized for passive cavitation detection) focus (co-aligned) was situated 5 mm behind the phantom front interface and at the front of the channel, with the transducers at a 90° angle to each other and 45° to the phantom (Figure 2B). Agent was held stationary in the channel and replenished for subsequent acquisitions.

Two arbitrary waveform generators (Tektronix AFG3022B) were used to drive the transmit transducer (1MHz, 1" diameter, 1.63" focal length; C302-SU, Olympus NDT, USA). One of these was used to control pulsing parameters, while the second one was used to trigger pulses of set parameters for a set number of repetitions. The transmit transducer was driven at varied peak negative pressures (100 – 1000 kPa; calibrated with a 200 µm aperture hydrophone as in Figure 2C; HGL-0200, Onda Corporation, USA) for a pulse duration of 100 µs at a pulse repetition period of 1 ms repeated 100 times (n = 4 interrogations per pressure). Pulses were amplified by a 55 dB linear power amplifier (A150, E&I Inc, USA) prior to being sent to the transmit transducer. Agent scattering in the phantom was then passively detected with a broadband piezocomposite 750 kHz focused receive transducer (1" diameter, 2" focal length; IL0758HP, Valpey-Fisher, USA), filtered (50 MHz low-pass filter; Minicircuits, USA), and digitized at 125 MHz with a 14-bit PC-based oscilloscope (PicoScope 6402C, Pico Technology Ltd).

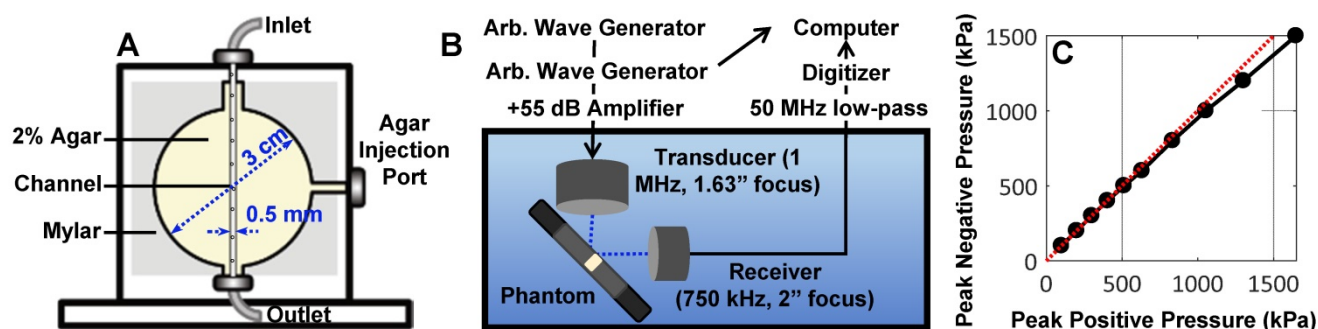


Figure 2. Overview of the benchtop acoustic scattering studies. (A) Schematic of channel phantom (0.5 mm diameter) intended to mimic a large vessel surrounded by tissue (2% agar gel). **(B)** Experimental configuration for passive cavitation detection of ultrasound-stimulated NBs in the phantom. **(C)** Hydrophone measurements of peak negative versus peak positive pressure at the transducer focus. These calibrations were utilized to assess NB scattering in the phantom as a function of pressure.

Tumor cell line and animal preparation

Green fluorescent protein (GFP) tagged human FaDu squamous cell carcinoma cells (AntiCancer Inc.) were cultured in 5% CO₂/95% air at 37 °C. Cells were propagated in RPMI medium 1640 with L-glutamine (MultiCell Technologies Inc.), supplemented with 10% FBS, 100 U/mL penicillin, and 100 µg/mL streptomycin, and were trypsinized and harvested prior to confluency. All animal procedures were approved and conducted in compliance with the Animal Care Committee guidelines at Sunnybrook Research Institute, Canada. Six- to eight-week old BALB/c nude mice (Charles River) underwent dorsal skinfold window chamber implantation as in [50, 52]. This technique involved the surgical implantation of a titanium frame to support the dorsal skinfold within a transparent window (Figure 3A). The upper layer of the dorsal skin was removed, and 2x10⁶ tumor cells in 30 µL of media were injected with a 30 G needle into the fascia in the window center, and a cover slip was placed over the opening (n = 15 mice). For inclusion in the study, mice with injected tumor cells were required to have both large visual regions of tumor cells within the volume-of-view, as well as noticeably affected (tortuous and redundant) vasculature (Figure 3B). Healthy mice were also utilized as vascular controls, where the dorsal chamber was implanted but no cells were injected (n = 5 mice), with noticeably straighter and less dense vasculature (Figure 3C). Studies were performed 8-10 days later.

For experiments, mice were anesthetized with isoflurane, and the tail vein was cannulated with a 27 G catheter. Mice were then placed on a heating pad on a removable microscope stage to maintain a core body temperature of 37 °C with feedback from a rectal thermistor (TC-1000; CWE Inc.). The window chamber coverslip was removed, the underlying exposed skinfold was wet with degassed saline, and a new 12 mm diameter, 150 µm thick coverslip with an in-house lead zirconate titanate (PZT-4) ring transducer fixed with cyanoacrylate adhesive to the

top surface was placed overtop the exposed skin and held in the chamber with an internal retaining ring (Figure 3D). The underside of the window chamber was coupled by ultrasound gel to a degassed water bath reservoir heated with a circulating water heater (T/Pump Model TP-500; Gaymar) to maintain the dorsal skinfold temperature at 37 °C. On the bottom of the reservoir was an in-house polyvinylidene difluoride (PVDF) receive transducer for passive acoustic monitoring (Figure 3E). The stage was then transferred to the multiphoton microscope for the study.

Multiphoton microscope settings

A water immersion 25x 1.05 NA objective lens with a field-of-view (FOV) of 509 µm x 509 µm (XLPN 25x, NA 1.05; Olympus) was positioned over the dorsal window chamber. Laser scanning was performed at 900 nm with a multiphoton microscope (FV1000MPE; Olympus) and a mode-locked Titanium Sapphire tunable laser (690-1040 nm; MaiTai Spectra-Physics). Fluorescent emissions following bandpass filtering were collected by a photomultiplier tube following bandpass filtering of 410-460 nm for collagen and 495-540 nm for FaDu-GFP, or by gallium arsenide phosphide (GaAsP) detectors following bandpass filtering of 575-645 nm for Texas Red tagged NBs.

Ultrasound parameters

An in-house lead zirconate titanate (PZT-4) ring transducer [53] was matched to a 50 Ω impedance, 0° phase load with a custom matching circuit, with a driving frequency of 1.13±0.07 MHz in thickness mode. The ring transducer was calibrated with a 75 µm aperture hydrophone (model NH0075, Precision Acoustics) in a degassed water bath with the same configuration as the experiment (i.e. air-backed with a droplet of degassed water in the inner part of the cylinder, coupled with a water-immersion lens and held within a titanium frame).

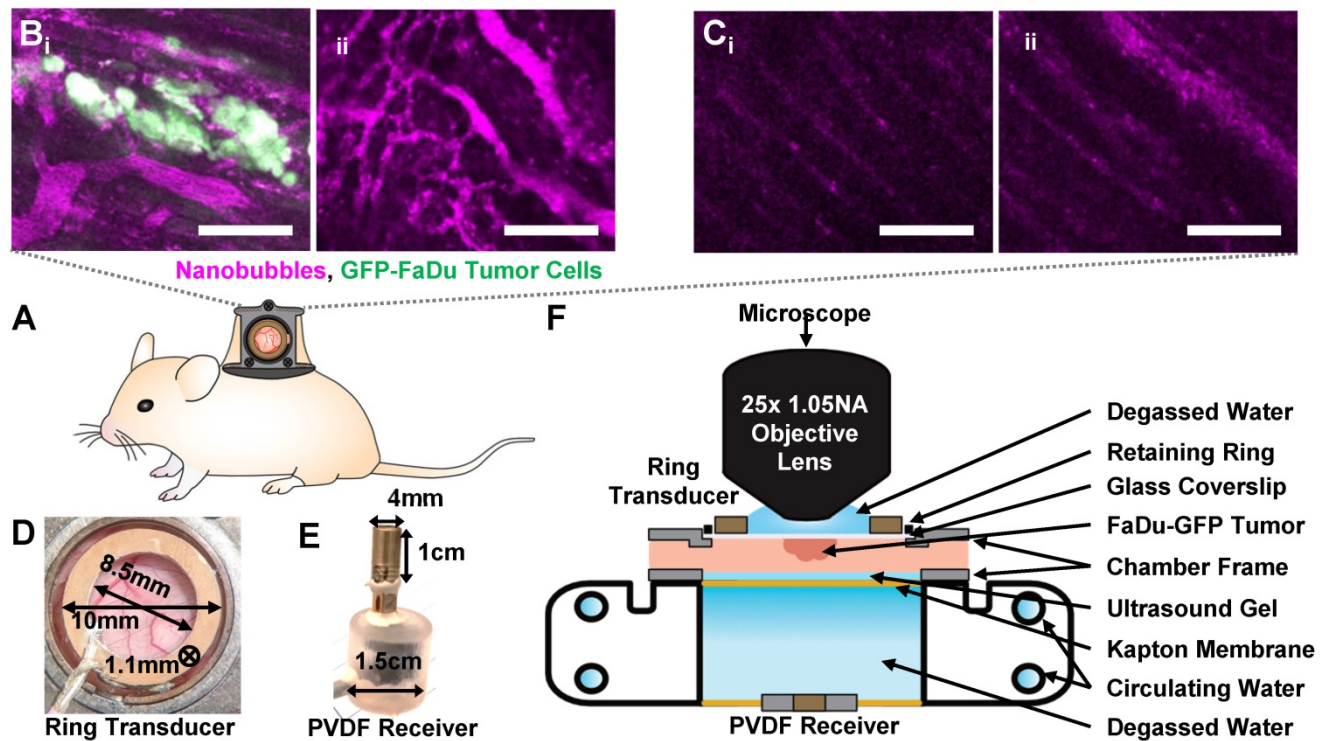


Figure 3. Overview schematic of the integrated acoustic and dorsal window chamber microscopy setup. (A) Side-view sketch of a mouse with a dorsal window chamber implanted, with a ring transducer and coverslip held in the window with a retaining ring. (B) Images of tumor tissue with dense tumor cell beds and noticeable vessel tortuosity. (C) Images of healthy tissue, with aligned, regular, straight vessels. Scale bar = 100 μm . (D) Photograph of the ring transducer held in the window chamber enabling acoustic stimulation during imaging, with dimensions. (E) Photograph of the acoustic receiver for detecting acoustic emissions behind the dorsal chamber, with dimensions. (F) Schematic of the multiphoton microscope interfacing with the dorsal window chamber and ultrasound transmit and receive transducers.

For sonication, the ring transducer was air-backed, with a droplet of degassed water in the inner part of the cylinder for compatibility with the water-immersion lens. Two arbitrary waveform generators (Tektronix AFG3022B) were used to drive the ring transducer. One of these was used to control pulsing parameters, while the second one was used to trigger pulses of set parameters for a set number of repetitions. Three different pulsing schemes were utilized. ‘Probe’ pulses were employed to assess the acoustic vascular kinetics of the NBs. Probes were sent at the ring transducer fundamental frequency at 300 kPa peak negative pressure with a pulse length of 100 μs , pulse repetition period (PRP) of 4 s to allow vascular replenishment, 5 times. ‘Destructive probe’ pulses were used to assess whether NBs extravasated intact. Destructive probes were sent at 1 MPa peak negative pressure with a pulse length of 100 μs , PRP of 10 ms, 50 times. After the first hit, a 10 s waiting period was utilized to enable possible vascular replenishment, after which a second hit was transmitted. ‘Sonication’ pulses were intended to enhance vascular permeability to increase delivery. Sonication pulses were sent at 500 kPa peak negative pressure 10 s after agent injection with a pulse length of 2.5 ms, a PRP of 4 s to allow for vascular replenishment, to 2 min (30 bursts).

Pulses were first attenuated by 20 dB, amplified with a 53 dB RF power amplifier (E&I Ltd.), filtered by a 3 MHz low-pass filter, and transmitted through the matching circuit to the ring transducer. Passive cavitation detection was achieved with an in-house broadband polyvinylidene fluoride (PVDF) receiver centred at 10 MHz. Receive signals were digitized at 125 MHz with a 14-bit PC-based oscilloscope (PicoScope 6402C, Pico Technology Ltd).

In vivo experimental procedure

As in [52, 50], the objective lens and ring transducer were colocalized and imaging was completed near the surface of the dorsal skinfold (up to a depth of 150 μm) to both maintain a high signal-to-noise ratio for the microscope and remain close to the transducer acoustic focus (with a lateral FWHM of $\sim 500 \mu\text{m}$). Prior to agent injections and laser scanning, baseline cavitation data was acquired with the same pulse sequences as would be utilized later. An injection of 0.1 mL TR-NBs at a concentration of $8 \times 10^8 \text{ mL}^{-1}$ followed by a 0.08 mL saline flush was then administered via the tail vein catheter, and a baseline XYZ volume stack was acquired to create a 3D tumor vascular map. Volume stacks were acquired with 512×512 pixels ($509.12 \mu\text{m} \times 509.12 \mu\text{m}$, resolution of $0.9944 \mu\text{m}/\text{pixel}$) to a Z-depth of 0-150

μm in $1 \mu\text{m}$ increments at $2 \mu\text{s}/\text{pixel}$. A second injection was performed 30 min after baseline acquisitions, marking the start time ($t=0$) of the experiments.

Two different experimental schemes were utilized (**Figure 4**): The first scheme ($n = 10$ mice) was intended to determine the vascular acoustic pharmacokinetic profile of the NBs, and to test whether NBs extravasated intact. In this scheme, probe pulses (300 kPa, $100 \mu\text{s}$ pulse length, 4 s PRP, 5x) were sent at 2, 5, 10, 15, 20, 30, and 40 min after injection. At 35 min, destructive probe pulses (1 MPa, $100 \mu\text{s}$ pulse length, PRP 10s, 50x; repeated after 10 s waiting period) were transmitted to acoustically determine if NBs extravasated intact. This scheme was also performed in healthy control mice ($n = 5$), to demonstrate that extravasation does not passively occur in the absence of leaky tumor vasculature. The second scheme ($n = 5$ mice) was utilized to assess whether ultrasound stimulation of NBs upon injection could actively enhance vascular permeability to increase delivery and determine whether there is a resultant increase in intact extravascular NBs. For this sequence, sonication pulses (500 kPa, 2.5 ms pulse length, 4 s PRP, 30x) were delivered 10 s after injection. These parameters are within range of those shown to give rise to drug delivery in conjunction with microbubbles.

During sonication, a time XYT stack (512x512 pixels, $2 \mu\text{s}/\text{pixel}$; the same lateral and temporal resolution as the volume stacks) was acquired at a pre-selected tissue plane of depth between 50-100 μm such that tumor vessels of various sizes could be visualized with good SNR for 3 min. At 35 min, destructive probe pulses were transmitted to acoustically probe for the presence of intact extravascular NBs following active (ultrasound-mediated) delivery. This scheme was also performed in healthy control mice ($n = 2$), to demonstrate the extent of ultrasound-NB-mediated delivery in tumor compared to healthy vasculature. Throughout both experimental schemes, volume scans were acquired to visually monitor possible extravasation and vascular effects for up to 40 min following injection.

Multiphoton microscopy data analysis

Multiphoton fluorescence images were analyzed in MATLAB with the assumption that fluorescence is proportional to concentration. The 575-645 nm channel (corresponding to NB signal) was corrected for GFP bleed-through, median filtered in 3-dimensions, and contrast enhanced via contrast-limited adaptive histogram equalization. A binarized 3D vessel mask from the baseline volume stack was created through iterative thresholding. Intra- and extra-vascular compartments were then

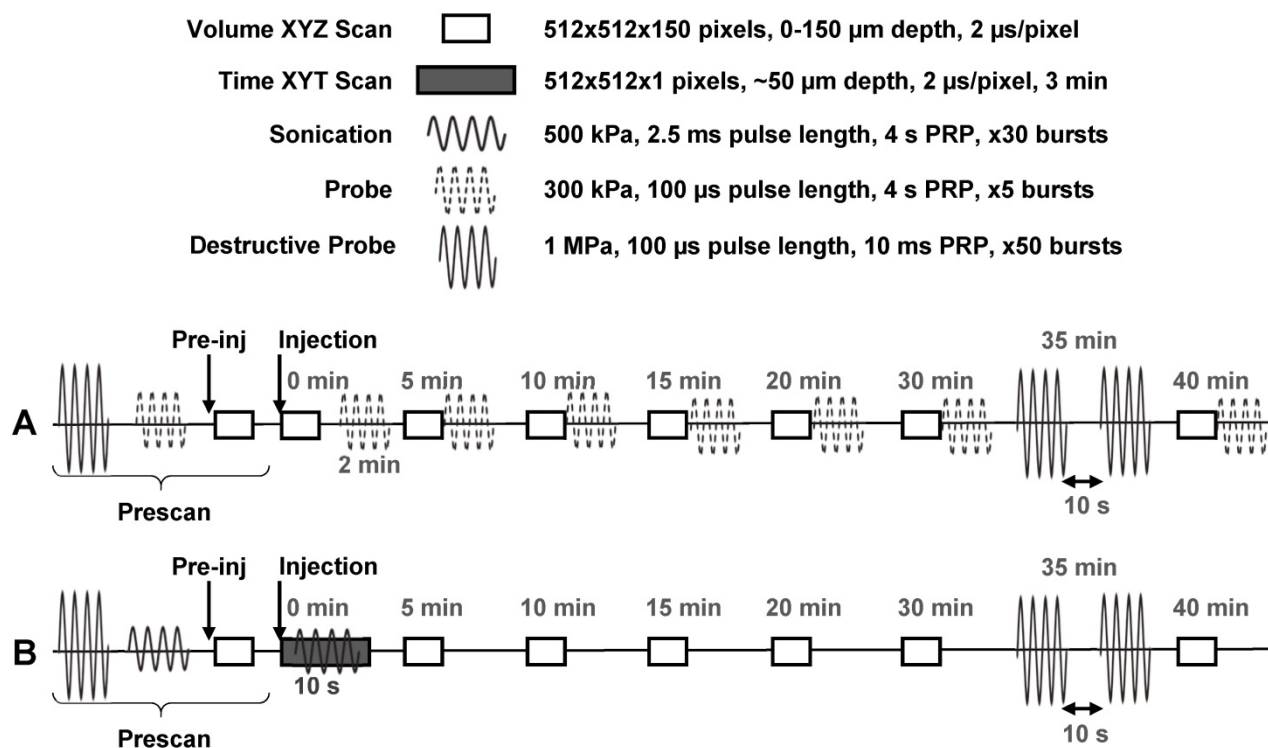


Figure 4. In vivo experimental timing diagram. (A) Scheme utilized to determine the vascular acoustic pharmacokinetic profile of the NBs, and test whether NBs extravasated intact ($n = 10$ mice with tumors, $n = 5$ healthy controls). (B) Scheme used to assess whether ultrasound stimulation of NBs upon injection can actively enhance vascular permeability to increase delivery; and whether there is a resultant increase in intact extravascular NBs ($n = 5$ mice with tumors, $n = 2$ healthy controls).

segmented for spatiotemporal analysis by applying the mask and its inverse to the longitudinal images acquired, respectively. A Euclidean distance transform of the segmented 3D vascular mask was then performed to create a distance map from each extravascular pixel to the nearest vascular structure and applied to the extravascular compartment. Boundary effects were removed by truncating the volume by 40 pixels on all sides. Extravascular compartment fluorescence was normalized with respect to the compartment volume at each distance away from the nearest vessel, and to baseline fluorescence (time 0 min, distance 0-2 μm).

In the sonication group, triggered drug release over the time-course of ultrasound exposure was additionally examined, with the caveat that this could only be assessed within a pre-selected tissue plane depth. Here, the first 10 frames of the time XYT stack (5.18 s; prior to sonication) of the pre-selected tissue plane depth were utilized to create a 2D vascular mask. This mask was applied to the stack to assess the increase in extravascular compartment fluorescence over time normalized with respect to compartmental volume and baseline fluorescence (frames 1-10). All data is displayed as the mean and standard deviation unless otherwise indicated.

Cavitation data analysis

Acoustic data was post-processed in MATLAB. Receive signals were digitally filtered (0.3 MHz high-pass and 5 MHz low-pass; 5th order bandpass Butterworth filter) and multiplied by a Hanning window of 50 μs length. For benchtop experiments, the Hanning window was centred on the received 100 μs signal. For *in vivo* experiments, the window was set to begin from the start of the received signal for the 2.5 ms sonication scheme; and was centered on the received signal for the 100 μs probe and destructive probe schemes. Windowed received signals were then zero-padded to a frequency resolution of 12.5 kHz per division prior to computing the Fourier transform and normalizing to the maximum received power in the first burst. For benchtop experiments, power spectra were then integrated over the fundamental frequency, 2nd harmonic, subharmonic, and inertial cavitation (between the fundamental and first ultraharmonic frequencies) bands with a bandwidth of -6 dB of the main lobe. For *in vivo* experiments, power spectra were integrated over the fundamental frequency and 2nd harmonic with a bandwidth of -6 dB of the main lobe. All data is displayed as the mean and standard deviation unless otherwise indicated. Significance was evaluated by a one-way analysis of variance (ANOVA) and a multiple comparison test.

Results and Discussion

Nanobubbles exhibit sustained nonlinear acoustic scattering

Despite the growing use of NBs, only a few studies have directly examined NB acoustic scattering systematically with a view to developing relevant ultrasound schemes [54, 55]. In these works, scattering of dilute (10^6 mL^{-1}) suspensions of porphyrin-lipid NBs was assessed, and found to initiate nonlinear scattering in a pressure threshold-dependent manner at low (3-8 MHz) [54] and high [55] (12.5-30 MHz) frequencies. Another study assessed a higher concentration (10^9 mL^{-1}) of NBs incorporating propylene glycol and glycerol similar to the NBs in this study, and found contrast enhancement at 7-12 MHz over pressures ranging from 245-465 kPa [34].

In this work, NBs were formulated with a membrane of contrasting elastic properties [34]. The compliant phospholipid encapsulating layer included propylene glycol as an edge activator for increased deformation [56-58], and glycerol as a membrane stiffener to increase buckling [59]. The formulation was further doped with lipid-conjugated Texas Red for fluorescent tracking. The agent size distribution was determined with a 10 μm aperture Multisizer 4e (measuring 0.2 - 6 μm ; Beckman Coulter Inc.) to be uncontaminated by larger particles which would dominate scattering, and to have number and volume distribution modes of 0.303 and 0.392 μm , respectively ($n = 3$; **Figure 1**).

NB scattering in response to ultrasound was assessed at a clinically relevant low concentration (10^6 mL^{-1}) in a vessel phantom (0.5 mm diameter). This low number density is aligned with current clinically acceptable microbubble doses based on gas volume [60, 61]; the concentrations are therefore matched, but the NB dose here is of a lower gas volume (proportional to radius, r^3) and surface area (proportional to r^2). A calibrated custom setup (**Figure 2**) was utilized to determine behavior as a function of pressure (100-1500 kPa) with a driving frequency of 1 MHz, 100 μs pulse length, 1 ms pulse repetition period, for 100 successive bursts. Representative scattered power spectra are shown in **Figure 5A**. It should be noted that asymmetries arise due to nonlinear propagation at higher pressures (**Figure 2C**); at least a component of signals above $\sim 800 \text{ kPa}$ is due to nonlinear propagation as well as nonlinear scattering. The receiver is additionally a narrowband transducer with higher sensitivity at its fundamental frequency (750 kHz) and odd harmonics (2.25 MHz), thus inertial cavitation appears more prominent in these bands.

The fundamental and second and third harmonic responses are distinct at low pressures and increase with pressure. A subharmonic peak is also visible at and above 200 kPa, and broadband noise emerges at 400 kPa. A quantification of scattered signals as a function of pressure in the subharmonic, fundamental, second harmonic, and inertial cavitation regimes is shown in **Figure 5B-E**. At the fundamental frequency, power rises rapidly (100-500 kPa) and then more gradually (> 500 kPa) as a function of pressure. At the subharmonic and second harmonic, power begins to ascend quickly from 200-500 kPa, then begins to plateau. These plateaus occur with the emergence of broadband inertial cavitation above 400 kPa. It is thus evident that these NBs can exhibit nonlinear acoustic scattering at low concentrations and low-to-moderate pressures, and that they do so in a pressure-dependent manner that is similar to previous observations with other formulations [54, 55].

To assess signal persistence, scattering response as a function of successive pulses is shown in **Figure 5F**. At 200 kPa, the subharmonic and second harmonic are visible without the presence of broadband noise, though these harmonics are short-lived, decaying to noise levels after ~20 bursts at 200 and 300 kPa. These nonlinearities become more persistent at higher

pressures with increasing inertial cavitation as a function of pressure. NBs are therefore further capable of sustained cavitation, as well as inertial cavitation for therapeutic avenues.

Nanobubbles demonstrate extended acoustic vascular pharmacokinetics

Custom ultrasound transmitters and receivers were next integrated into a window chamber for simultaneous intravital optical and acoustic monitoring of intravenously injected NBs in tumor-affected microcirculation (**Figure 3**). First, NB acoustic vascular pharmacokinetics were assessed following passive infusion, in terms of their ability to initiate cavitation at a particular exposure level in plasma. The scheme utilized is outlined in **Figure 4A**: 100 μ s, 300 kPa probes were sent in a short series (x5) with a 4 s PRP at 2, 5, 10, 15, 20, 30, and 40 min following injection. The 4 s PRP enables vascular replenishment of agent, while the short pulse length and moderate 300 kPa pressure enable reliably distinct nonlinear scattering without the presence of inertial cavitation, based on benchtop results (**Figure 5**). Thus, probing pulses briefly check for cavitation from intact NBs in the vasculature without causing destruction or permeabilization.

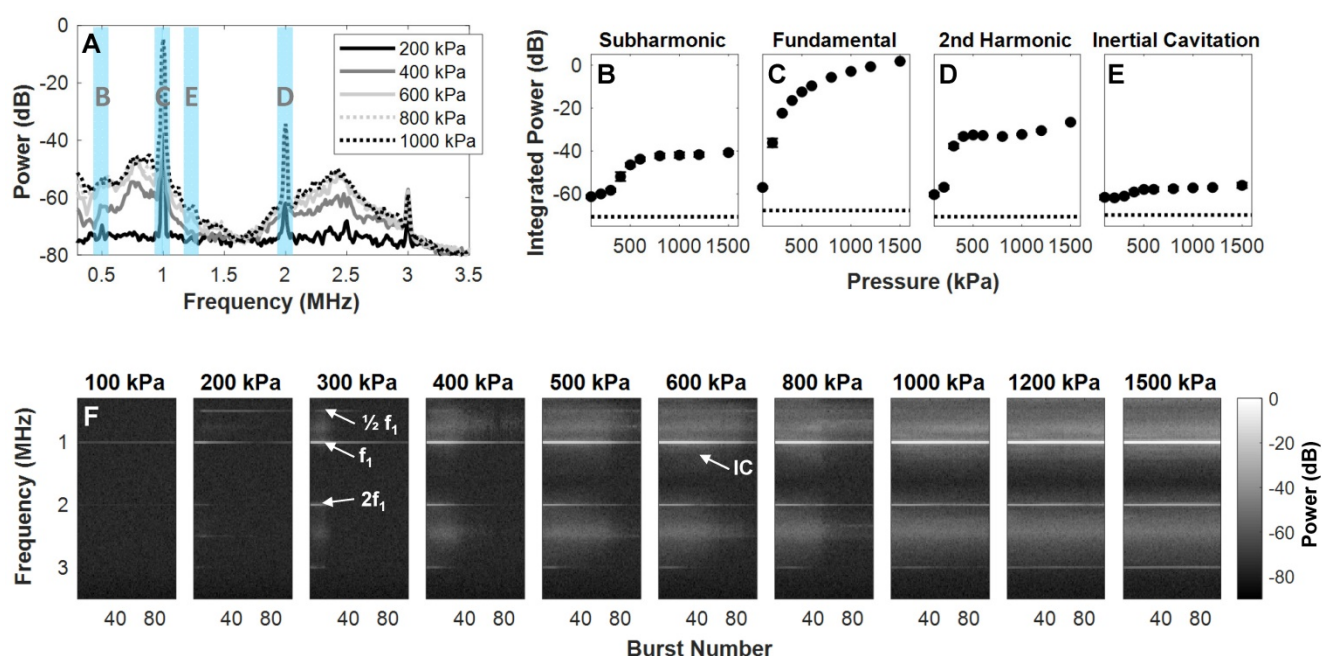


Figure 5. Pressure-dependent scattered power from NBs. (A) Representative received scattered power over a range of pressures. Highlighted regions denote frequency bands over which signals were integrated to calculate quantified scattering data in (B) subharmonic, (C) fundamental, (D) second harmonic, and (E) inertial cavitation regimes as a function of pressure. Data is averaged for the first 5 bursts of ultrasound exposure and over $n = 4$ interrogations per pressure. (F) NB power spectra as a function of successive bursts at different pressures (100-1500 kPa, in columns). Arrows denote the subharmonic ($1/2 f_1$), fundamental frequency (f_1), second harmonic ($2f_1$), and inertial cavitation (IC) regimes.

Figure 6A shows the acoustic vascular pharmacokinetic profile of a low concentration NB bolus in tumor and healthy tissue. Prior to injection, probing pulses detected no cavitation ($t=0$ min). After injection, probes detected strong cavitation activity that decayed back to baseline by 20 min. This is far longer than typical microbubble formulations at equivalent doses that last on the order of 30 s to 5 min as measured with conventional imaging methods [62-64], with the caveat that the acoustic pharmacokinetic profile here was assessed with a different pulsing scheme. Other NB studies have compared NBs and microbubbles under the same exposure conditions, matching gas volume or number density, and found that NBs were more stable [7, 32, 33].

Nanobubbles preferentially and passively extravasate intact into tumors

Following infusion, visual and acoustic data were utilized to determine whether NBs passively extravasate from tumor vasculature, and crucially, whether they extravasate intact. Works to date employ imaging of tumors or histology to demonstrate extravasation; however, the ultrasound imaging methods utilized did not have sufficient resolution to determine whether detected bubbles are truly outside of vessels, and histology simply depicts extravasated shell material.

Here, the scheme in **Figure 4A** provided visual monitoring of extravasation of material over time, with example images shown in **Figure 6B**. Fluorescence in the vascular and extravascular compartments of tumor and healthy tissue over time is quantified and shown in **Figure 6C**. Over a 40 min timespan from injection, there was preferential passive extravasation in tumors (up to 1.5x baseline) compared to healthy controls (1.15x). There was correspondingly a slightly greater decrease in intravascular fluorescence in tumor tissue. While visual intravital monitoring provides evidence of extravasation, it does so without distinguishing between intact NBs and shell fragments. While shell fragments can have relevance for imaging (if tagged) or therapy (if loaded appropriately), here we determine whether at least a subset of the visual data is associated with intact NBs for an extended range of applications.

To determine whether any NBs extravasated intact, destructive probes were applied at 35 min – after the lower amplitude imaging probes determined that NBs were no longer intact in the vasculature. Destructive probes consisted of two ‘hits’ with the same parameters; a short pulse length of 100 μ s at high pressure (1 MPa) with a short pulse repetition

period of 10 ms, 50 times. After the first hit a 10 s waiting period was utilized, after which a second hit was transmitted. The high pressure was selected to ensure broadband emissions (**Figure 5**) for detection of a potential lower number density, and because NBs in a confining tissue-like environment require higher pressures for cavitation [54]. The long waiting period between the hits enables possible vascular replenishment if the NBs are present in blood; if the first hit exhibits cavitation that quickly decays and does not return in the second hit, it would indicate the presence of intact NBs disrupted by the hits (i.e. extravascular stationary signal) rather than being replenished (i.e. vascular signal).

In **Figure 6D**, the first destructive probe pulse at 35 min did not detect cavitation in healthy controls, indicating the absence of intact NBs. In the tumor group, however, significant cavitation above baseline was elicited, that was not detectable 10 s later. Specifically, the first destructive probe hit yielded strong elevated power at the fundamental frequency, second-, third-, and sub-harmonics that decayed with rapid successive hits (**Figure 6E**) and did not return 10 s later after possible replenishment. This indicates the presence of stationary, intact NBs in the extravascular space of tumors that were destroyed during the first hit. With the same reasoning, it has been shown that NBs can be generated *in situ* from ultrasound-stimulated microbubbles and be actively delivered intact into the extravascular compartment [50]. This is the first study to demonstrate that NBs passively extravasate intact with contained gas in tumors. Maintaining gas content in the extravascular compartment is crucial to fully realize the potential of NBs: For imaging, extravasating NBs can facilitate detection of leakage due to disease processes (tumors, insulinitis, *etc.*) and detect cell-surface markers in tissue. From a therapeutic perspective, extravascular NBs can initiate cavitation-based therapy approaches deeper in tumor tissue and in closer proximity to tumor cells.

Ultrasound stimulation actively enhances delivery of intact nanobubbles

While we have demonstrated that NBs passively extravasate intact in a preclinical tumor model, the enhanced permeability and retention effect has been clinically disputed [65]. Therefore, NBs were next stimulated with ultrasound (500 kPa, 2.5 ms pulse length, 4 s pulse repetition period, 2 min total duration) upon injection to actively enhance blood-tissue permeability. These parameters are within range of those shown to give rise to drug delivery in conjunction with microbubbles, and are the same as those used in the previous simultaneous

intravital and acoustic monitoring study that investigated the generation and extravasation of intact nanobubbles from ultrasound-stimulated microbubbles [50]. Here the scheme in **Figure 4B** provided monitoring both over the timescale of the sonication (at a pre-selected depth) and beyond over the entire FOV.

Over the timescale of the sonication (2 min), fluorescence in the extravascular compartment underwent a rapid rise to 1.5x its initial state in a pre-selected tissue plane in mice with tumors (**Figure 7A**). Acoustic monitoring during sonication (**Figure 7B,C**) denotes nonlinear scattering in the subharmonic and first ultraharmonic frequency bands that decay within a few bursts, as well as distinct elevated

fundamental and second harmonics that persist. The lack of broadband noise implies that ultrasound-mediated active delivery was initiated under stable cavitation conditions. This is an important finding, as more violent inertial cavitation is often associated with hemorrhage and edema [66].

Over a longer timescale after sonication, extravascular fluorescence continued to increase to an average of 3x its initial state in mice with tumors, and to 1.6x its initial state in healthy mice (**Figure 8A**). Therefore, sonication of NBs for 2 min beginning 10 s post-injection actively enhances extravasation in both tumor and healthy groups, though to a greater extent in tumor tissue.

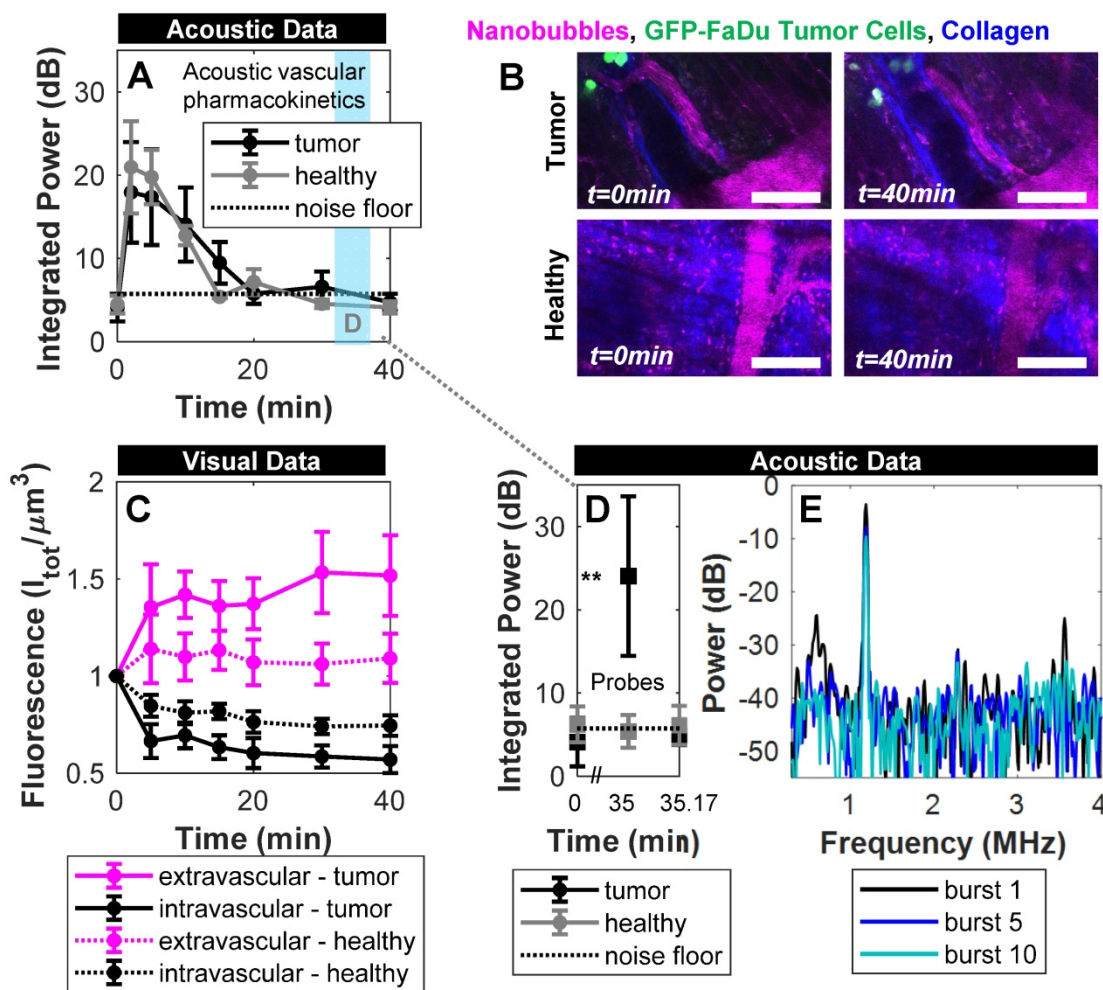


Figure 6. Acoustic and visual tracking of NBs under passive delivery conditions. (A) Acoustic vascular pharmacokinetic profile demonstrating the decay in acoustic integrated power as a function of time in tumor (n = 10) and healthy (n = 5) vasculature. Periodic probes (300 kPa, 100 μs, 4 s pulse repetition period, 5 bursts) detect NB cavitation *in vivo* for 20 min following injection. **(B)** Multiphoton images of NBs in tumor-affected and healthy vasculature over the course of passive delivery. A decrease in intravascular fluorescence and slight increase in extravascular fluorescence emerges slowly over 40 min, preferentially in tumor tissue. Scale bar = 100 μm. **(C)** Fluorescent tracking and vascular segmentation demonstrate preferential passive delivery of NBs to the extravascular compartment (volume of 509 μm × 509 μm × 150 μm) in tumors compared to healthy tissue. **(D)** Destructive probe pulse data (1000 kPa, 100 μs, 10 ms pulse repetition period, 50 bursts) intended to check for intact NBs in the extravascular compartment detected significant cavitation (** p<0.01) above baseline at 35 min in tumor vasculature, which is not detectable 10 s later due to destruction of stationary NBs. Conversely, destructive probe pulses did not detect cavitation above baseline in healthy mice. **(E)** Power spectra for the 1st, 5th, and 10th burst in the first destructive probe sequence at 35 min. Elevated power at the fundamental frequency, second-, third-, and sub-harmonics are visible in the 1st burst and decay with subsequent exposure.

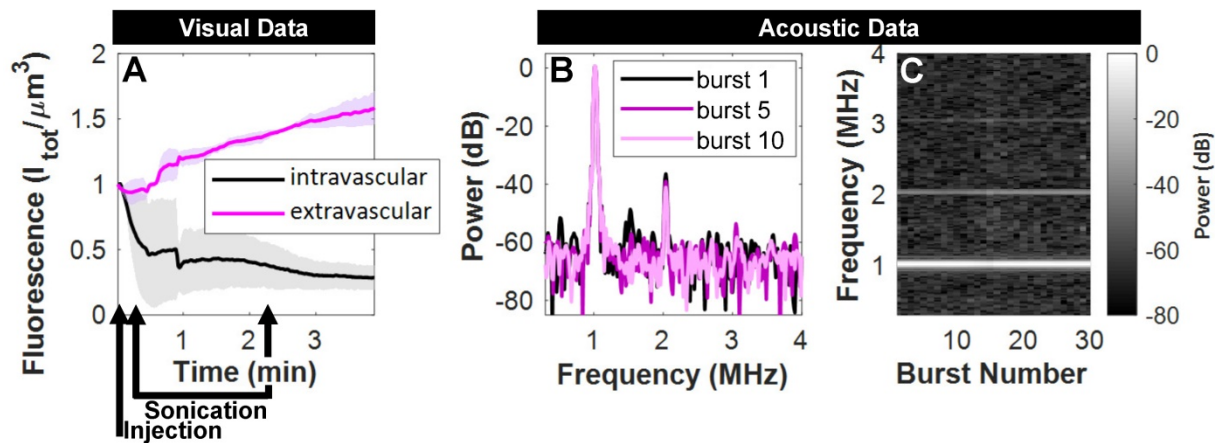


Figure 7. Acoustic and visual monitoring during ultrasound-stimulation of NBs. (A) Fluorescent tracking demonstrates a rapid rise in signal in the extravascular compartment upon sonication in mice with tumors. Visual data at this time resolution required pre-selection of a tissue plane, and is averaged here for the cases where vascular disruption was captured at this depth (n = 3/5). (B) Acoustic monitoring during sonication (500 kPa, 2.5 ms, 4 s pulse repetition period, 2 min total duration) demonstrates scattered power in the subharmonic and first ultraharmonic frequency bands in the first burst that is not visible thereafter, as well as distinct elevated fundamental and second harmonics that (C) persist over the duration of ultrasound-stimulation.

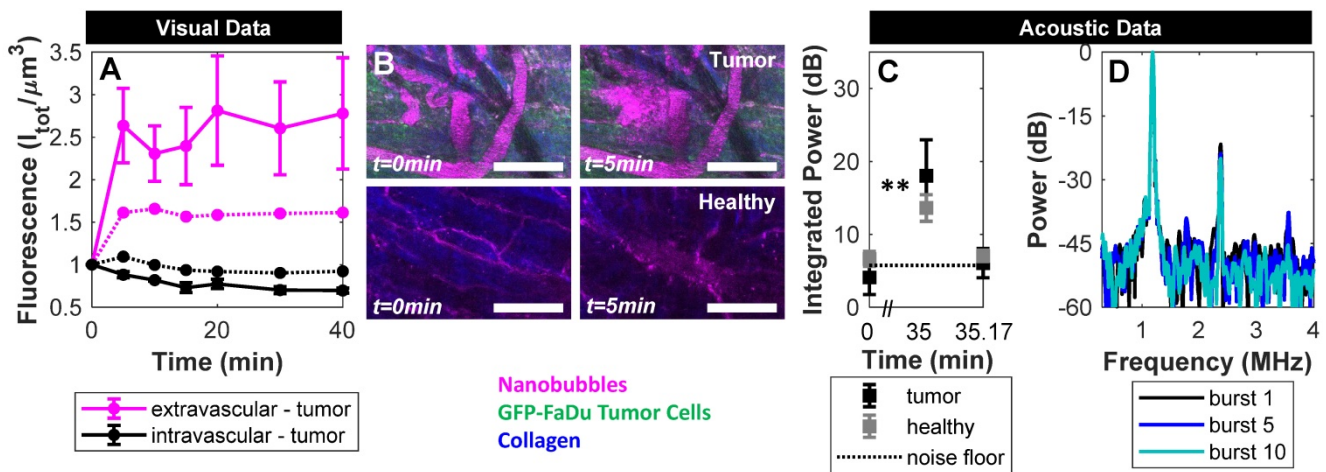


Figure 8. Acoustic and visual tracking of NBs upon ultrasound-mediated active delivery. (A) Fluorescent tracking illustrates a rapid rise in signal in the extravascular compartment during and immediately following sonication, followed by a plateau over the entire volume FOV. Sonication of NBs for 2 min beginning 10 s post-injection actively enhances extravasation in tumor (n = 5) and healthy (n = 2) groups, though to a greater extent in tumor tissue. (B) Representative images of ultrasound-mediated delivery in tumor and healthy tissue. Scale bar = 100 μm. (C) Destructive probe pulse data (1000 kPa, 100 μs, 10 ms pulse repetition period, 50 bursts) intended to check for intact NBs in the extravascular compartment detected significant cavitation above baseline at 35 min in both tumor (** p<0.01) and healthy groups following ultrasound-mediated active delivery. (D) Power spectra for the 1st, 5th, and 10th burst in the first destructive probe sequence at 35 min following active delivery. Elevated power at the fundamental frequency, second-, third-, and first ultra-harmonics are visible in the 1st burst and decay with subsequent exposure.

This visual data provides evidence of actively enhanced delivery of fluorescently labelled shell material which is of relevance for the use of drug-loaded NBs. However, this does not distinguish between shell fragments or intact NBs. To determine whether ultrasound-based active delivery enhanced intact NB delivery to the extravascular compartment, destructive probes (two ‘hits’ of 1 MPa, 100 μs pulse length, 10 ms pulse repetition period, 50 times; 10 s apart) were again utilized at 35 min. In **Figure 8C**, the first destructive probe pulse detected significant cavitation above baseline in tumor and healthy groups. This is indicative of the presence of intact NBs upon ultrasound-mediated active delivery. Cavitation levels in the active delivery groups (tumor-affected and healthy), however, were not significantly

different, nor were levels comparing active and passive delivery to tumor-affected mice. Spatiotemporal extravasation was notably different between active and passive delivery to tumor-affected mice (**Figure 9A, B**), with ultrasound-mediated active delivery resulting in greatly enhanced extravasation distances.

While destructive probes do not provide spatial information on detected cavitation, aside from that inferred from behavior and time delays, it is possible that active delivery enhances intact NB penetration into tumors under the tested conditions: Indeed it has recently been shown that targeted NBs under ultrasound exposure are able to achieve deep penetration into rabbit clots, and with greater efficacy than stimulated MBs [67]. Ultrasound stimulation of

NBs has also been shown to enhance delivery and penetration of co-injected or loaded drugs in various preclinical tumor models [10, 11, 48, 49] and for blood-brain-barrier disruption [7, 8], though intact NB extravasation was not validated and microscale events were not visualized. A plethora of ultrasound parameters have been used, typically with frequencies between 1-10 MHz, durations on the order of a few minutes, but greatly varying acoustic pressures from 100 kPa to several MPa. The penetrating capacity of intact NBs warrants further investigation with a wider set of ultrasound parameters and a more advanced array receiver setup capable of more accurately localizing extravasated NBs. However, it should be noted that even with precise signal localization many factors will affect scattering. Scattered power will depend on NB concentration, proximity to other bubbles, NB diameter and nonlinear shell rheology, as well as microscopic local environment mechanical properties. Thus further exploration is warranted, yet will still require other concurrent monitoring methods (such as intravital multiphoton microscopy applied here).

Ultrasound stimulation of nanobubbles elicits a range of biological effects

The integrated intravital visual and acoustic setup further provides powerful spatiotemporal insights. Such real-time monitoring of acute vascular effects resulting from ultrasound-stimulated bubble-based therapeutic approaches has only been utilized in a handful of studies in simplified models [68-70], in the absence of tumors [71-73], and without [52, 71-73] or with [50] recording acoustic response. However, these studies utilized microbubbles; no study to date has provided real-time intravital monitoring of acute vascular effects upon ultrasound

stimulation of NBs. The events detailed below are further the first reported microscale observations of NB-vessel interactions in a complex tissue model (beyond glass catfish and the chorioallantoic membrane) outside of the brain.

While anecdotal, **Figure 10** depicts a range of captured NB-vessel interactions during or following ultrasound exposure. To provide context for the relative incidence of these events, we note that a range of 20-50 vessels were visible within the FOV of any given mouse. A total of $n = 5$ mice with tumor-affected vasculature were studied under ultrasound stimulation with 153 total vessels, and $n = 2$ healthy mice were assessed with 86 total vessels. None of the visualized events were observed in tumor or healthy mice in the absence of ultrasound exposure ($n = 10$ tumor, $n = 5$ healthy mice).

Two types of vascular disruption were visualized; rapid focal leakage (**Figure 10A**) which occurred during sonication, and slow widespread leakage (**Figure 10B**) occurring shortly following exposure. Microbubble-mediated vascular permeabilization for locally enhanced transport is one of the most widely studied therapeutic applications of ultrasound [5, 74, 75], and has advanced to clinical trials for transient blood-brain-barrier disruption [76] and enhanced delivery to tumors [77]. Microbubble-mediated permeabilization can be achieved *via* thermal (hyperthermia) or mechanical (sonoporation, endocytosis) mechanisms [78]. Microbubble oscillation-driven fluid flow (microstreaming, microjets) [79] and acoustic radiation forces [80] then assist in drug transport across the permeabilized vessel wall into tissue. Direct microscopic observations of permeabilization of individual vessels has been conducted in a variety of preclinical models for microbubbles [50, 68-73]. This is

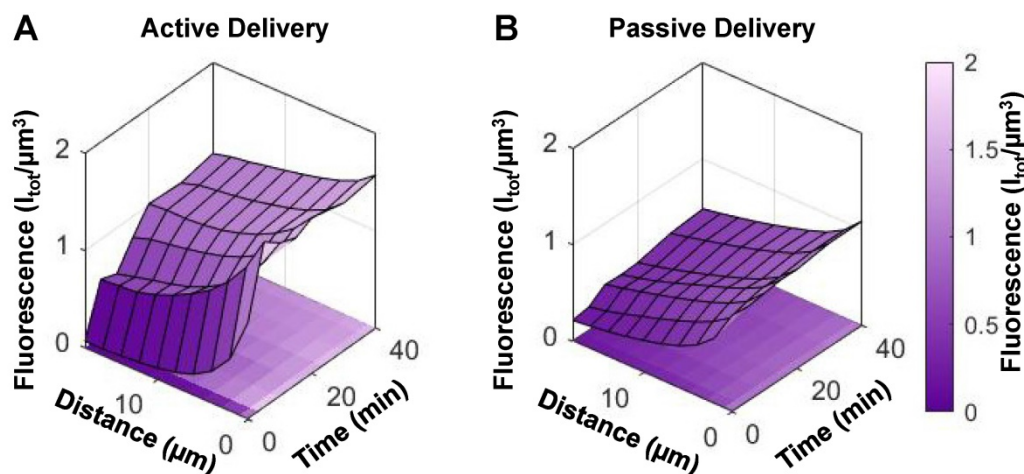


Figure 9. (A) Extravasation surface plot as a function of distance from the nearest vessel and time in mice with tumors that underwent active (ultrasound-mediated) delivery (mean of $n = 5$), and (B) passive delivery (mean of $n = 10$).

the first study to visualize vascular permeabilization with ultrasound-stimulated nanobubbles, capturing disruption in 18 vessels (11/153 tumor vessels, 7/86 healthy vessels) with fluorescence of extravasated NBs colocalized with tumor cells.

Vascular shutdown was also observed (**Figure 10C**) in vessels within a dense tumor bed during sonication (19/153 tumor vessels, 0/86 healthy vessel). Antivascular therapy has been achieved *via* continuous wave ultrasound with high microbubble concentrations (resulting in macroscopic temperature elevations) [81, 82], as well as lower duty cycle pulsed ultrasound [83–86] with both high [84, 87] and low [83, 85, 88] microbubble doses. Antivascular therapy can inhibit tumor growth [85, 86, 89] and has further been reported to have strong synergistic effects when combined with radiotherapy [84] and anticancer agents [86, 88, 90]. It is notable that the pressures and mechanical indices employed for the pulsed ultrasound work was higher than that in the present study. The role of bubble size on this approach has yet to be investigated, though these effects have been shown to be achievable with submicron bubbles [91].

In **Figure 10D**, agent was observed to either be taken up into or ‘sonoprinted’ onto endothelial cells of

the vessel wall (observed in 22 vessels; 18/153 tumor vessels, 4/86 healthy vessels). This behavior has been reported with ultrasound-stimulated microbubbles using pressures above 300 kPa and short pulses [92, 93], as well as during stable cavitation with more moderate pressures (100–300 kPa) and longer pulses [50, 93, 94], and involves imprinting of shell material onto endothelial cells. This visual pattern notably remains the same before and after higher pressure destructive probe pulses, and results in similar cavitation levels regardless of incidence, and is therefore hypothesized to not contain gas. With this study being the first to employ intravital imaging of ultrasound-stimulated NBs, this is also the first report of sonoprinting with NBs.

In **Figure 10E**, 30–40 min after injection and exposure, agent appeared to either coalesce together, or alternatively attach to red blood cells in the vascular compartment. This was found to occur long after dissolution of gas from NBs in the vasculature and could contribute to the plateau in extravasation. This behavior was relatively rare, however (occurring in 4 tumor-affected vessels in 1 animal) and should be studied further.

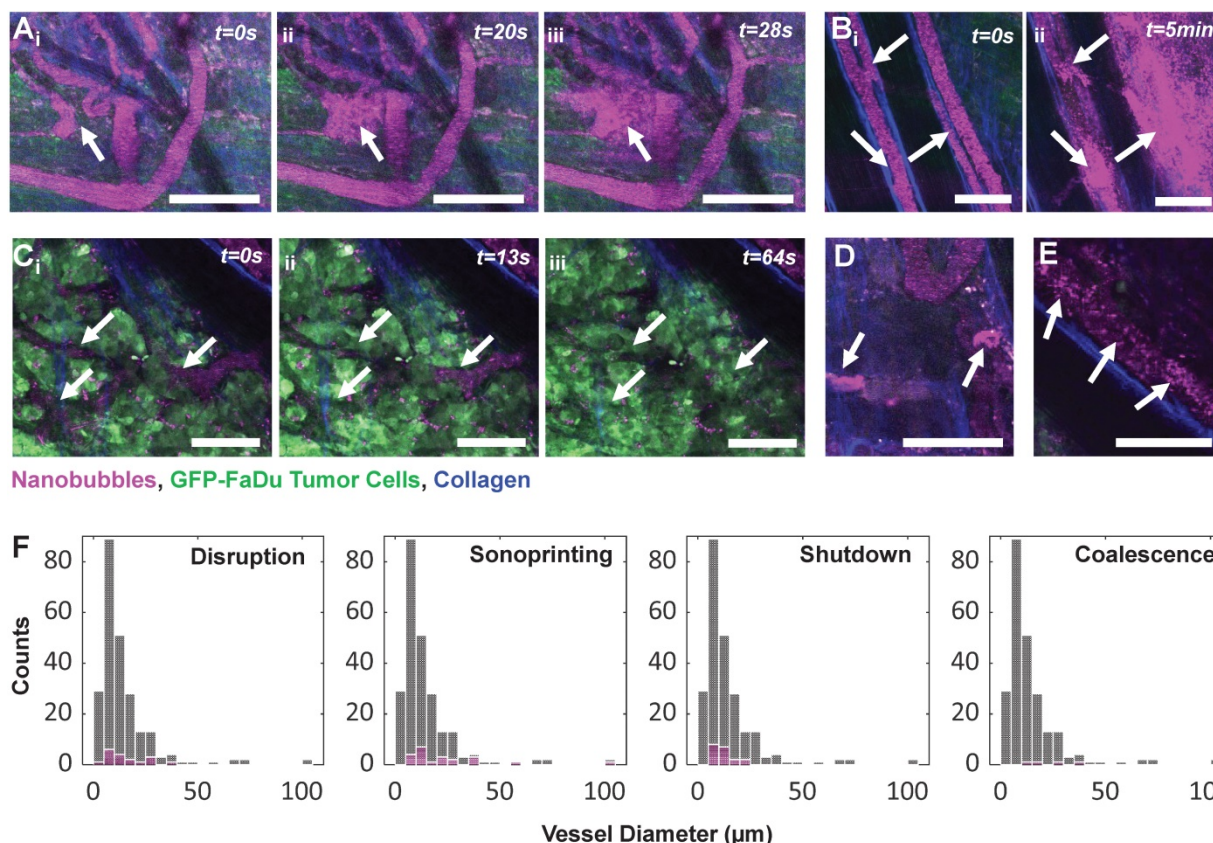


Figure 10. NB-vessel interactions visualized with intravital multiphoton microscopy. Fluorescent agent is colorized magenta, GFP-tagged FaDu tumor cells are green, and collagen is blue. **(A)** Rapid (within seconds) focal vascular disruption during ultrasound exposure (which begins at $t=10$ s). **(B)** Slower (within minutes), widespread vascular permeabilization occurring following ultrasound exposure. **(C)** Time-series depicting vascular shutdown in vessels within a dense tumor bed during sonication. **(D)** Stationary agent in vessels 25 min following injection and sonication, indicating uptake into or sonoprinting onto endothelial cells of the vessel wall. **(E)** Distinct moving clusters of agent signal 40 min following injection and exposure, hypothesized to be due to agent coalescence or attachment to red blood cells. Scale bar = 100 μm . **(F)** Histograms of vascular events (pink) organized by vessel diameter and event type, superimposed on total visualized vessels (gray).

While these biological effects were varied and phenomenological in nature, they all occurred under the same exposure conditions (500 kPa, 2.5 ms pulse length, 4 s pulse repetition period, 2 min total duration). The sonication parameters and injected bubble concentration were also utilized in a prior study of ultrasound stimulation of microbubbles to generate and facilitate the delivery of NBs to tumors [50]. In the aforementioned work, extravascular fluorescence increased 5x, cavitation in accordance with stationary extravascular NBs was detected, and the spatial release profile was far greater than passive controls [50]. Ultrasound stimulation for active delivery further occurred under stable cavitation conditions [50], as in the present study. In the current work, extravascular fluorescence increased by 3x under the same conditions with an equivalent number density of NBs (and therefore has a correspondingly lower gas volume and surface area doses). In both works, fluorescence was tracked *via* a tagged shell and thus corresponds to surface area of the bubbles, with 10 % fluorophore doping in the microbubble case, and 0.9 % doping in the NBs. With both cases occurring under stable cavitation and fewer vascular effects being observed in the present NB study, it is likely that a direct comparison of microbubbles and NBs with matched surface area content and fluorophore doping would result in greater delivery efficacy for NBs with fewer adverse events.

Microbubbles and NBs have been directly compared in a delivery context *in vivo* in only two works, both of which were for blood-brain-barrier opening: Bing *et al.* compared NBs to clinical microbubble formulations Optison® and Definity™ under similar total gas volumes, with 0.5 MHz focused ultrasound and pressures ranging from 0.1 – 0.7 MPa with acoustic feedback control [7]. It was found that NBs could achieve more reliable opening, though no histology was provided to compare resultant damage [7]. Fan *et al.* compared NBs to the clinical microbubble formulation SonoVue®, with 1 and 10 MHz focused ultrasound and pressures ranging from 0.5 – 4.5 MPa [8]. It was found that NBs achieved blood-brain-barrier opening with less hemorrhagic damage *via* histology, though it is unclear whether the two bubble groups were matched in terms of concentration or gas volume [8]. Both of these studies were unable to monitor effects in real-time, highlighting the potential utility of the integrated optical and acoustic setup presented here for high temporal and spatial resolution observations of ultrasound-stimulated NBs.

Conclusion

The present study has sought to gain insights

into NBs and their potential for accessing the tumor extravascular space intact. NBs formulated with contrasting membrane elasticity architecture were found to exhibit sustained nonlinear acoustic scattering at clinically relevant low concentration (10^6 mL⁻¹) and frequency (1 MHz), over a range of pressures (100-1500 kPa). Simultaneous intravital optical and acoustic monitoring revealed that these NBs yield a lengthy acoustic vascular pharmacokinetic profile (20 min). It was then demonstrated that NBs preferentially and passively extravasate intact with contained gas into tumors (1.5x baseline) compared to healthy tissue (1.15x), and that ultrasound-stimulation further enhances their delivery (5x) and spatial bioavailability. Finally, ultrasound-stimulation of NBs was found to elicit a range of biological effects that either have not been previously reported or directly observed with NBs. These insights substantiate the immense potential that NBs can offer for extending ultrasound-based applications beyond the vascular compartment.

Abbreviations

2D: two-dimensional; 3D: three-dimensional; ANOVA: analysis of variance; DHPE: 1,2-dihexadecanoyl-*sn*-glycero-3-phosphoethanolamine; DBPC: 1,2-dibehenoyl-*sn*-glycero-3-phosphocholine; DPPE: 1,2-dipalmitoyl-*sn*-glycero-3-phosphoethanolamine; DPPA: 1,2-dipalmitoyl-*sn*-glycero-3-phosphate; DSPE-mPEG2k: 1,2-distearoyl-*sn*-glycero-3-phosphoethanolamine-*N*-[methoxy(polyethylene glycol)-2000]; FOV: field of view; GaAsP: gallium arsenide phosphide; GFP: green fluorescent protein; NB: nanobubble; PVDF: polyvinylidene difluoride; PZT-4: lead zirconate titanate.

Acknowledgments

The authors thank S. Bulner for performing tumor cell culture; V. Chan and S. Rideout-Gros for performing the dorsal skinfold window chamber implantation surgeries; A. Wright for his assistance in calibrating the ring transducers; M. A. O'Reilly for fabricating the PVDF receive transducer; and A. Dorr for her support in using the multiphoton microscope. E. C. A. and A. A. E. acknowledge support from the National Institute of Biomedical Imaging and Bioengineering of the National Institutes of Health (NIH grant no. R01EB025741), and the Office of the Assistant Secretary of Defense for Health Affairs through the Prostate Cancer Research Program (DoD award no. W81XWH-16-1-0371). Views and opinions of, and endorsements by the authors do not reflect those of the National Institutes of Health or of the Department of Defense. C. P., G. Z., and D. E. G. acknowledge support by the Canadian Institutes for

Health Research, Natural Sciences and Engineering Research Council of Canada, Prostate Cancer Canada, Terry Fox Research Institute, Canada Foundation for Innovation, Canada Research Chairs Program, Princess Margaret Cancer Foundation, and the Vanier Canada Graduate Scholarship.

Author Contributions

C. P., A. A. E., G. Z., and D. E. G. conceived of the experiments. E. C. A. fabricated the agent used. C. P. characterized the agent, conducted benchtop and *in vivo* experiments, and analyzed all data under the guidance of A. A. E., G. Z., and D. E. G. The manuscript was written by C. P. with contributions from all authors. All authors have approved the final version of the manuscript.

Competing Interests

The authors have declared that no competing interest exists.

References

- Appis AW, Tracy MJ, Feinstein SB. Update on the safety and efficacy of commercial ultrasound contrast agents in cardiac applications. *Echo Res Pract.* 2015; 2: 55-62.
- Sidhu PS, Choi BI, Nielsen MB. The EFSUMB guidelines on the non-hepatic clinical applications of contrast enhanced ultrasound (CEUS): a new dawn for the escalating use of this ubiquitous technique. *Ultraschall Med.* 2012; 33: 5-7.
- Sirsi S, Borden M. Microbubble compositions, properties and biomedical applications. *Bubble Sci Eng Technol.* 2009; 1: 3-17.
- Leighton TG. *The Acoustic Bubble.* San Diego: Academic Press. 1994.
- Goertz DE. An overview of the influence of therapeutic ultrasound exposures on the vasculature: high intensity ultrasound and microbubble-mediated bioeffects. *Int J Hyperthermia.* 2015; 31: 134-144.
- Goertz DE, Frijlink ME, de Jong N, van der Steen AFW. High frequency nonlinear scattering from a micrometer to submicrometer sized lipid encapsulated contrast agent. *Ultrasound Med Biol.* 2006; 32: 569-577.
- Bing C, Hong Y, Hernandez C, Rich M, Cheng B, Munaweera I, et al. Characterization of different bubble formulations for blood-brain barrier opening using a focused ultrasound system with acoustic feedback control. *Sci Rep.* 2018; 8: 1-12.
- Fan CH, Liu HL, Ting CY, Lee YH, Huang CY, Ma YJ, et al. Submicron-bubble-enhanced focused ultrasound for blood-brain barrier disruption and improved CNS drug delivery. *PLoS One.* 2014; 9: e96327.
- Wu M, Zhao H, Guo L, Wang Y, Song J, Zhao X, et al. Ultrasound-mediated nanobubble destruction (UMND) facilitates the delivery of A10-3.2 aptamer targeted and siRNA-loaded cationic nanobubbles for therapy of prostate cancer. *Drug Deliv.* 2018; 25: 226-240.
- Yu Z, Wang Y, Xu D, Zhu L, Hu M, Liu Q et al. G250 antigen-targeting drug-loaded nanobubbles combined with ultrasound targeted nanobubble destruction: A potential novel treatment for renal cell carcinoma. *Int J Nanomed.* 2020; 15: 81-95.
- Kida H, Nishimura K, Ogawa K, Watanabe A, Feril LB, Irie Y, et al. Nanobubble mediated gene delivery in conjunction with a hand-held ultrasound scanner. *Front Pharmacol.* 2020; 11: 363.
- Cavalli R, Bisazza A, Giustetto P, Civra A, Lembo D, Trotta G, et al. Preparation and characterization of dextran nanobubbles for oxygen delivery. *Int J Pharm.* 2009; 381: 160-165.
- Argenziano M, Banche G, Luginini A, Finesso N, Allizond V, Gulino GR, et al. Vancomycin-loaded nanobubbles: A new platform for controlled antibiotic delivery against methicillin-resistant *Staphylococcus Aureus* infections. *Int J Pharm.* 2017; 523: 176-188.
- Kwan JJ, Myers R, Covellio CM, Grahan SM, Shah AR, Stride E, et al. Ultrasound-propelled nanocups for drug delivery. *Small.* 2015; 11: 5305-5314.
- Kripfgans OD, Fowlkes JB, Miller DL, Eldevik OP, Carson PL. Acoustic droplet vaporization for therapeutic and diagnostic applications. *Ultrasound Med Biol.* 2000; 26: 1177-1189.
- Pellow C, Goertz DE, Zheng G. Breaking free from vascular confinement: status and prospects for submicron ultrasound contrast agents. *Wiley Interdiscip Rev Nanomed Nanobiotechnol.* 2017; 10: e1502.
- Paul S, Russakow D, Nahire R, Nandy T, Ambre AH, Katti K, et al. In vitro measurement of attenuation and nonlinear scattering from echogenic liposomes. *Ultrason.* 2012; 52: 962-969.
- Alkan-Onyuksel H, Demos SM, Lanza GM, Vonesh MJ, Klegerman ME, Kane BJ, et al. Development of inherently echogenic liposomes as an ultrasonic contrast agent. *J Pharm Sci.* 1996; 85: 486-490.
- Radhakrishnan K, Haworth KJ, Huang SL, Klegerman ME, McPherson DD, Holland CK. Stability of echogenic liposomes as a blood pool ultrasound contrast agent in a physiologic flow phantom. *Ultrasound Med Biol.* 2012; 38: 1970-1981.
- Xia L, Karandish F, Kumar KN, Froberg J, Kulkarni P, Gange KN, et al. Acoustic characterization of echogenic polymersomes prepared from amphiphilic block copolymers. *Ultrasound Med Biol.* 2018; 44: 447-457.
- Walsby AE. Gas Vesicles. *Microbiol Rev.* 1994; 58: 94-144.
- Shapiro MG, Goodwill PW, Neogy A, Yin M, Foster FS, Schaffer DV, et al. Biogenic gas nanostructures as ultrasonic molecular reporters. *Nat Nanotechnol.* 2014; 9: 311-316.
- Maresca D, Lakshmanan A, Lee-Gosselin A, Melis JM, Ni YL, Bourdeau RW, et al. Nonlinear ultrasound imaging of nanoscale acoustic biomolecules. *Appl Phys Lett.* 2017; 110: 073704.
- Yildirim A, Chattaraj R, Blum NT, Goodwin AP. Understanding acoustic cavitation initiation by porous nanoparticles: toward nanoscale agents for ultrasound imaging and therapy. *Chem Mater.* 2016; 28: 5962-5972.
- Sheeran P, Matsuura N, Borden MA, Williams R, Matsunaga TO, Burns PN, et al. Methods of generating submicrometer phase-shift perfluorocarbon droplets for applications in medical ultrasonography. *IEEE Trans Ultrason Ferroelectr Freq Control.* 2017; 64: 252-263.
- Rapoport N. Phase-shift, stimuli-responsive perfluorocarbon nanodroplets for drug delivery to cancer. *Wiley Interdiscip Rev Nanomed Nanobiotechnol.* 2012; 4: 492-510.
- Cavalli R, Soster M, Argenziano M. Nanobubbles: A promising efficient tool for therapeutic delivery. *Ther Deliv.* 2016; 7: 117-138.
- Perera RH, Hernandez C, Zhou H, Kota P, Burke A, Exner AA. Ultrasound imaging beyond the vasculature with new generation contrast agents. *Wiley Interdiscip Rev Nanomed Nanobiotechnol.* 2015; 7: 593-608.
- Cai WB, Yang HL, Zhang J, Yin JK, Yang YL, Yuan LJ, et al. The optimized fabrication of nanobubbles as ultrasound contrast agents for tumor imaging. *Sci Rep.* 2015; 5: 13725.
- Goertz DE, de Jong N, van der Steen AFW. Attenuation and size distribution measurements of Definity and manipulated Definity populations. *Ultrasound Med Biol.* 2007; 33: 1376-1388.
- Krupka TM, Solorio L, Wilson RE, Wu H, Azar N, Exner AA. Formulation and characterization of echogenic lipid-Pluronic nanobubbles. *Mol Pharm.* 2010; 7: 49-59.
- Wu H, Rognin NG, Krupka TM, Solorio L, Yoshiara H, Guenette G, et al. Acoustic characterization and pharmacokinetic analyses of new nanobubble ultrasound contrast agents. *Ultrasound Med Biol.* 2013; 39: 2137-2146.
- Wu H, Abenojar EC, Perera R, de Leon AC, An T, Exner AA. Time-intensity-curve analysis and tumor extravasation of nanobubble ultrasound contrast agents. *Ultrasound Med Biol.* 2019; 45: 2502-2514.
- de Leon A, Perera R, Hernandez C, Cooley M, Jung O, Jeganathan S, et al. Contrast enhanced ultrasound imaging by nature-inspired ultrastable echogenic nanobubbles. *Nanoscale.* 2019; 11: 15647-15658.
- Shang M, Wang K, Guo L, Duan S, Lu Z, Li J. Development of novel ST68/PLA-PEG stabilized ultrasound nanobubbles for potential tumor imaging and theranostic. *Ultrason.* 2019; 99: 105947.
- Zhang J, Wei L, Zhao Y. Synthesis of nanobubbles for improved ultrasound tumor-imaging applications. *3 Biotech.* 2019; 10: 12.
- Hernandez C, Lilly J, Fioravanti G, Hadley J, Exner AA. Ultrasound signal from sub-micron lipid-coated bubbles. *IEEE Int Ultrason Symp.* 2017.
- Yin T, Wang P, Zheng R, Zheng B, Cheng D, Zhang X, et al. Nanobubbles for enhanced ultrasound imaging of tumors. *Int J Nanomed.* 2012; 7: 895-904.
- Wheatley MA, Forsberg F, Dube N, Patel M, Oeffinger BE. Surfactant-stabilized contrast agent on the nanoscale for diagnostic ultrasound imaging. *Ultrasound Med Biol.* 2006; 32: 83-93.
- Liu R, Tang J, Xu Y, Dai Z. Bioluminescence imaging of inflammation in vivo based on bioluminescence and fluorescence resonance energy transfer using nanobubble ultrasound contrast agent. *ACS Nano.* 2019; 13: 5124-5132.

41. Peyman SA, McLaughlin JR, Abou-Saleh RH, Marston G, Johnson BRG, Freear S, et al. On-chip preparation of nanoscale contrast agents towards high-resolution ultrasound imaging. *Lab Chip*. 2016; 16: 679-687.
42. Gao Y, Hernandez C, Yuan HX, Lilly J, Kota P, Zhou H, et al. Ultrasound molecular imaging of ovarian cancer with CA-125 targeted nanobubble contrast agents. *Nanomed*. 2017; 7: 2159-2168.
43. Yang H, Cai W, Xu L, Lv X, Qiao Y, Li P, et al. Nanobubble-affibody: Novel ultrasound contrast agents for targeted molecular ultrasound imaging of tumor. *Biomater*. 2014; 37: 279-288.
44. Zhang X, Wu M, Zhang Y, Zhang J, Su J, Yang C. Molecular imaging of atherosclerotic plaque with lipid nanobubbles as targeted ultrasound contrast agents. *Colloids Surf B Biointerfaces*. 2020; 189: 110861.
45. Ramirez DG, Abenojar E, Hernandez C, Lorberbaum DS, Papazian LA, Passman S, et al. Contrast-enhanced ultrasound with sub-micron sized contrast agents detects insulinitis in mouse models of type1 diabetes. *Nat Comm*. 2020; 11: 2238.
46. Bosca F, Bielecki PA, Exner AA, Barge A. Porphyrin-loaded Pluronic nanobubbles: A new ultrasound-activated agent for future theranostic applications. *Bioconjug Chem*. 2018; 29: 234-240.
47. Hu C, Wu M, Zhang R, Jiang D, Wang J. Ultrasound-mediated nanobubble destruction (UMND) facilitates the delivery of VEGFR2-targeted CD-TK-loaded cationic nanobubbles in the treatment of bladder cancer. *J Canc Res Clin Oncol*. 2020; 146: 3.
48. Zhong S, Ling Z, Zhou Z, He J, Ran H, Wang Z, et al. Herceptin-decorated paclitaxel-loaded poly(lactide-co-glycolide) nanobubbles: Ultrasound-facilitated release and targeted accumulation in breast cancers. *Pharm Dev Technol*. 2019; 25: 454-463.
49. Nittayacharn P, Yuan HX, Hernandez C, Bielecki P, Zhou H, Exner AA. Enhancing tumor drug distribution with ultrasound-triggered nanobubbles. *J Pharm Sci*. 2019; 108: 3091-3098.
50. Pellow C, O'Reilly MA, Hynynen K, Zheng G, Goertz DE. Simultaneous intravital optical and acoustic monitoring of ultrasound-triggered nanobubble generation and extravasation. *Nano Lett*. 2020; 20: 4512-4519.
51. Nittayacharn P, Dai K, de Leon A, Therdrattawong C, Exner AA. The effect of freeze/thawing on the physical properties and acoustic performance of perfluoropropane nanobubble suspensions. *IEEE Int Ultrason Symp*. 2019.
52. Santos MA, Goertz DE, Hynynen K. Focused ultrasound hyperthermia mediated drug delivery using thermosensitive liposomes and visualized with in vivo two-photon microscopy. *Theranostics*. 2017; 7: 2718-2731.
53. Nhan T, Burgess A, Hynynen K. Transducer design and characterization for dorsal-based ultrasound exposure and two-photon imaging of in vivo blood-brain barrier disruption in a rat model. *IEEE Trans Ultrason Ferroelectr Freq Contr*. 2013; 60: 1376-1385.
54. Pellow C, Acconcia C, Zheng G, Goertz DE. Threshold-dependent nonlinear scattering from porphyrin nanobubbles for vascular and extravascular applications. *Phys Med Biol*. 2018; 63: 215001.
55. Pellow C, Tan J, Cherin E, Demore CEM, Zheng G, Goertz DE. High frequency ultrasound nonlinear scattering from porphyrin nanobubbles. *Ultrason*, in press. doi: 10.1016/j.ultras.2020.106245.
56. Demetzos C, Pispas S, Pippa N. Drug delivery nanosystems: From bioinspiration and biomimetics to clinical applications. Singapore: Pan Stanford Publishing Pte Ltd. 2019.
57. Elmoslemany RM, Abdallah OY, El-Khordagui LK, Khalafallah NM. Propylene glycol liposomes as a topical delivery system for miconazole nitrate: Comparison with conventional liposomes. *AAPS Pharm Sci Tech*. 2012; 13: 723-731.
58. El-Maghraby GM, Barry BW, Williams AC. Liposomes and skin: From drug delivery to model membranes. *Eur J Pharm Sci*. 2008; 4: 203-222.
59. Pocivavsek L, Gavrilov K, Cao KD, Chi EY, Li D, Lin B, et al. Glycerol-induced membrane stiffening: The role of viscous fluid adlayers. *Biophys J*. 2011; 101: 118-127.
60. Morel DR, Schwieger I, Hohn L, Terrettaz J, Llull JB, Cornioley YA, et al. Human pharmacokinetics and safety evaluation of SonoVue, a new contrast agent for ultrasound imaging. *Invest Radiol*. 2000; 35: 80-85.
61. Abdelmoneim SS, Mulvagh SL. Perflutren lipid microsphere injectable suspension for cardiac ultrasound. *Imaging Med*. 2012; 4: 171-191.
62. Goertz DE, Wright C, Hynynen K. Contrast agent kinetics in the rabbit brain during exposure to therapeutic ultrasound. *Ultrasound Med Biol*. 2012; 36: 916-924.
63. Bouakaz A, Versluis M, de Jong N. High-speed optical observations of contrast agent destruction. *Ultrasound Med Biol*. 2005; 31: 391-399.
64. Wu SK, Chu PC, Chai WY, Kang ST, Tsai CH, Fan CH, et al. Characterization of different microbubbles in assisting focused ultrasound-induced blood-brain barrier opening. *Sci Rep*. 2017; 7: 46689.
65. Lanza GM, Moonen C, Baker JJ, Chang E, Cheng Z, Grodzinski P, et al. Assessing the barriers to image-guided drug delivery. *Wiley Interdiscip Rev Nanomed Nanobiotechnol*. 2014; 6: 1-14.
66. Skyba DM, Price RJ, Linka AZ, Skalak TC, Kaul S. Direct in vivo visualization of intravascular destruction of microbubbles by ultrasound and its local effects on tissue. *Circulation*. 1998; 98: 290-293.
67. Ma L, Wang Y, Zhang S, Qian X, Xue N, Jiang Z, et al. Deep penetration of targeted nanobubbles enhanced cavitation effect on thrombolytic capacity. *Bioconjug Chem*. 2020; 31: 369-374.
68. Faez T, Skachkov I, Versluis M, Kooiman K, de Jong N. In vivo characterization of ultrasound contrast agents: microbubble spectroscopy in a chicken embryo. *Ultrasound Med Biol*. 2012; 38: 1608-1617.
69. Tarapacki C, Kuebler WM, Tabuchi A, Karshafian R. Reversible and irreversible vascular bioeffects induced by ultrasound and microbubbles in chorioallantoic membrane model. *Proc 14th Int Symp Therap Ultras*. 2017; 1821:1-5.
70. Maruvada S, Hynynen K. Optical monitoring of ultrasound-induced bioeffects in glass catfish. *Ultrasound Med Biol*. 2004; 30: 67-74.
71. Cho EE, Drazic J, Ganguly M, Stefanovic B, Hynynen K. Two-photon fluorescence microscopy study of cerebrovascular dynamics in ultrasound-induced blood-brain barrier opening. *J Cereb Blood Flow Metab*. 2011; 31: 1852-1862.
72. Nhan T, Burgess A, Cho EE, Stefanovic B, Lilje L, Hynynen K. Drug delivery to the brain by focused ultrasound induced blood-brain barrier disruption: Quantitative evaluation of enhanced permeability of cerebral vasculature using two-photon microscopy. *J Control Release*. 2013; 172: 274-280.
73. Raymond SB, Skoch J, Hynynen K, Backsai BJ. Multiphoton imaging of ultrasound/Optison mediated cerebrovascular effects in vivo. *J Cereb Blood Flow Metab*. 2007; 27: 393-403.
74. Kooiman K, Vos HJ, Versluis M, de Jong N. Acoustic behavior of microbubbles and implications for drug delivery. *Adv Drug Del Rev*. 2014; 72: 28-48.
75. Deckers R, Moonen CTW. Ultrasound triggered, image guided, local drug delivery. *J Control Release*. 2010; 148: 25-33.
76. Mainprize T, Lipsman N, Huang Y, Meng Y, Bethune A, Ironside S, et al. Blood-brain barrier opening in primary brain tumors with non-invasive MR-guided focused ultrasound: a clinical safety and feasibility study. *Sci Rep*. 2019; 9: 1-7.
77. Dimcevski G, Kotopoulos S, Bjanec T, Hoem D, Schjott J, Gjertsen BT, et al. A human clinical trial using ultrasound and microbubbles to enhance gemcitabine treatment of inoperable pancreatic cancer. *J Control Release*. 2016; 243: 172-181.
78. Goertz DE. An overview of the influence of therapeutic ultrasound exposures on the vasculature: High intensity ultrasound and microbubble-mediated bioeffects. *Int J Hyperthermia*. 2015; 31: 134-144.
79. Caskey CF, Stieger SM, Qin S, Dayton PA, Ferrara KW. Direct observations of ultrasound microbubble contrast agent interaction with the microvessel wall. *J Acoust Soc Am*. 2007; 122: 1191-1200.
80. Kokhius TJA, Skachkov I, Naaijken BA, Juffermans LJM, Kamp O, Kooiman K, et al. Intravital microscopy of localized stem cell delivery using microbubbles and acoustic radiation force. *Biotechnol Bioeng*. 2015; 112: 220-227.
81. Wood AKW, Ansaloni S, Ziemer LS, Lee WMF, Feldman MD, Sehgal CM. The antivasular action of physiotherapy ultrasound on murine tumors. *Ultrasound Med Biol*. 2005; 31: 1403-1410.
82. Wood A, Bunte R, Price H, Deitz M, Tsai J, Lee W, et al. The disruption of murine tumor neovasculature by low-intensity ultrasound - comparison between 1 MHz and 3 MHz sonication frequencies. *Acad Radiol*. 2009; 15: 1133-1141.
83. Burke CW, Klivanov AL, Sheehan JP, Price RJ. Inhibition of glioma growth by microbubble activation in a subcutaneous model using low duty cycle ultrasound without significant heating. *J Neurosurg*. 2011; 114: 1654-1661.
84. Czarnota GJ, Karshafian R, Burns PN, Wong S, Al Mahrouki A, Lee JW, et al. Tumor radiation response enhancement by acoustical stimulation of the vasculature. *Proc Natl Acad Sci USA*. 2012; 109: e2203-e2041.
85. Goertz DE, Karshafian R, Hynynen K. Antivasular effects of pulsed low intensity ultrasound and microbubbles in mouse tumors. *IEEE Ultrason Symp*. 2008; 1: 670-673.
86. Goertz DE, Todorova M, Mortazavi O, Agache V, Chen B, Karshafian R, et al. Antitumor effects of combining docetaxel (taxotere) with the antivasular action of ultrasound stimulated microbubbles. *PLoS One*. 2012; 7: e52307.
87. Wood AKW, Ansaloni S, Ziemer LS, Lee WMF, Feldman MD, Sehgal CM. The antivasular action of physiotherapy ultrasound on murine tumors. *Ultrasound Med Biol*. 2005; 31: 1403-1410.
88. Todorova M, Agache V, Mortazavi O, Chen B, Karshafian R, Hynynen K, et al. Antitumor effects of combining metronomic chemotherapy with the antivasular action of ultrasound stimulated microbubbles. *Int J Cancer*. 2013; 132: 2956-2966.

89. Wood AKW, Schultz SM, Lee WMF, Bunte RM, Sehgal CM. Antivascular ultrasound therapy extends survival of mice with implanted melanomas. *Ultrasound Med Biol.* 2010; 36: 853-857.
90. Bulner S, Prodeus A, Garipey J, Hynynen K, Goertz DE. Enhancing checkpoint inhibitor therapy with ultrasound stimulated microbubbles. *Ultrasound Med Biol.* 2019; 45: 500-512.
91. Matsuura N, Koonar E, Zhu S, Leung BYC, Seo M, Sivapalan N Goertz DE. Inducing antivascular effects in tumors with submicrometer bubbles. *IEEE Ultrason Symp.* 2015.
92. De Cock I, Lajoinie G, Versluis M, De Smedt SC, Lentacker I. Sonoprinting and the importance of microbubble loading for the ultrasound mediated cellular delivery of nanoparticles. *Biomater.* 2016; 83: 294-307.
93. Roovers S, Lajoinie G, De Cock I, Brans T, Dewitte H, Breckmans K, et al. Sonoprinting of nanoparticle-loaded microbubbles: Unraveling the multi-timescale mechanism. *Biomater.* 2019; 217: 119250.
94. Kooiman K, Foppen-Harteveld M, van der Steen AFW, de Jong N. Sonoporation of endothelial cells by vibrating targeted microbubbles. *J Control Release.* 2011; 154: 35-41.
95. Batchelor DVB, Abou-Saleh RH, Coletta PL, McLaughlin JR, Peyman SA, Evans SD. Nested nanobubbles for ultrasound-triggered drug release. *ACS Appl Mater Interfaces.* 2020; 12: 29085-29093.